Search for Solar ^{8}B Neutrinos in the PandaX-4T Experiment Using Neutrino-Nucleus Coherent Scattering

Wenbo Ma,[1] Abdusalam Abdukerim,[1] Chen Cheng,[2] Zihao Bo,[1] Wei Chen,[1] Xun Chen,[1,3] Yunhua Chen,[4] Zhaokan Cheng,[5] Xiangyi Cui,[6] Yingjie Fan,[7] Deqing Fang,[8] Changbo Fu,[8] Mengting Fu,[9] Lisheng Geng,[10,11,12] Karl Giboni,[1] Linhui Gu,[1] Xuyuan Guo,[4] Chencheng Han,[6] Ke Han,[1] Changda He,[1] Jinrong He,[4] Di Huang,[1] Yanlin Huang,[13] Zhou Huang,[1] Ruquan Hou,[3] Xiangdong Ji,[14] Yonglin Ju,[15] Chenxiang Li,[1] Jiafu Li,[2] Mingchuan Li,[4] Shu Li,[15] Shuaijie Li,[6] Qing Lin,[16,17,*] Jianglai Liu,[1,6,3,†] Xiaoying Lu,[18,19] Lingyin Luo,[9] Yunyang Luo,[17] Yugang Ma,[8] Yajun Mao,[9] Nasir Shaheed,[18,19] Yue Meng,[1,3,‡] Xuyang Ning,[1] Ningchun Qi,[4] Zhicheng Qian,[1] Xiangxiang Ren,[18,19] Changsong Shang,[4] Xiaofeng Shang,[1] Guofang Shen,[10] Lin Si,[1] Wenliang Sun,[4] Andi Tan,[14] Yi Tao,[1,3] Anqing Wang,[18,19] Meng Wang,[18,19] Qiuhong Wang,[8] Shaobo Wang,[1,20] Siguang Wang,[9] Wei Wang,[5,2] Xiuli Wang,[15] Zhou Wang,[1,3,6] Yuehuan Wei,[5] Mengmeng Wu,[2] Weihao Wu,[1] Jingkai Xia,[1] Mengjiao Xiao,[14] Xiang Xiao,[2] Pengwei Xie,[6] Binbin Yan,[1] Xiyu Yan,[13] Jijun Yang,[1] Yong Yang,[1] Chunxu Yu,[7] Jumin Yuan,[18,19] Ying Yuan,[1] Zhe Yuan,[8] Xinning Zeng,[1] Dan Zhang,[14] Minzhen Zhang,[1] Peng Zhang,[4] Shibo Zhang,[1] Shu Zhang,[2] Tao Zhang,[1] Yingxin Zhang,[18,19] Yuanyuan Zhang,[6] Li Zhao,[1] Qibin Zheng,[13] Jifang Zhou,[4] Ning Zhou,[1] Xiaopeng Zhou,[10] Yong Zhou,[4] and Yubo Zhou[1]

(PandaX Collaboration)

[1]*School of Physics and Astronomy, Shanghai Jiao Tong University, Key Laboratory for Particle Astrophysics and Cosmology (MoE), Shanghai Key Laboratory for Particle Physics and Cosmology, Shanghai 200240, China*
[2]*School of Physics, Sun Yat-Sen University, Guangzhou 510275, China*
[3]*Shanghai Jiao Tong University Sichuan Research Institute, Chengdu 610213, China*
[4]*Yalong River Hydropower Development Company, Ltd., 288 Shuanglin Road, Chengdu 610051, China*
[5]*Sino-French Institute of Nuclear Engineering and Technology, Sun Yat-Sen University, Zhuhai 519082, China*
[6]*Tsung-Dao Lee Institute, Shanghai Jiao Tong University, Shanghai 200240, China*
[7]*School of Physics, Nankai University, Tianjin 300071, China*
[8]*Key Laboratory of Nuclear Physics and Ion-beam Application (MOE), Institute of Modern Physics, Fudan University, Shanghai 200433, China*
[9]*School of Physics, Peking University, Beijing 100871, China*
[10]*School of Physics, Beihang University, Beijing 102206, China*
[11]*International Research Center for Nuclei and Particles in the Cosmos and Beijing Key Laboratory of Advanced Nuclear Materials and Physics, Beihang University, Beijing 100191, China*
[12]*School of Physics and Microelectronics, Zhengzhou University, Zhengzhou, Henan 450001, China*
[13]*School of Medical Instrument and Food Engineering, University of Shanghai for Science and Technology, Shanghai 200093, China*
[14]*Department of Physics, University of Maryland, College Park, Maryland 20742, USA*
[15]*School of Mechanical Engineering, Shanghai Jiao Tong University, Shanghai 200240, China*
[16]*State Key Laboratory of Particle Detection and Electronics, University of Science and Technology of China, Hefei 230026, China*
[17]*Department of Modern Physics, University of Science and Technology of China, Hefei 230026, China*
[18]*Research Center for Particle Science and Technology, Institute of Frontier and Interdisciplinary Science, Shandong University, Qingdao 266237, Shandong, China*
[19]*Key Laboratory of Particle Physics and Particle Irradiation of Ministry of Education, Shandong University, Qingdao 266237, Shandong, China*
[20]*SJTU Paris Elite Institute of Technology, Shanghai Jiao Tong University, Shanghai 200240, China*

(Received 7 July 2022; accepted 23 November 2022; published 11 January 2023)

A search for interactions from solar ^{8}B neutrinos elastically scattering off xenon nuclei using PandaX-4T commissioning data is reported. The energy threshold of this search is further lowered compared with the previous search for dark matter, with various techniques utilized to suppress the background that emerges from data with the lowered threshold. A blind analysis is performed on the data with an effective exposure

of 0.48 tonne year, and no significant excess of events is observed. Among the results obtained using the neutrino-nucleus coherent scattering, our results give the best constraint on the solar ^{8}B neutrino flux. We further provide a more stringent limit on the cross section between dark matter and nucleon in the mass range from 3 to 9 GeV/c^2.

DOI: 10.1103/PhysRevLett.130.021802

Because of complex fusion processes inside the Sun, neutrinos are continuously generated in large amount. As liquid xenon (LXe) detectors dedicated to dark matter (DM) direct search [1–3] have been developed into the multitonne scale in recent years, they are now able to reach the sensitivity to detect solar neutrinos via coherent elastic nuclear scattering (CEνNS). Among all sources of solar neutrinos, neutrinos produced in the β decay of ^{8}B are the most likely ones to be detected due to the 15 MeV Q value. The flux of ^{8}B solar neutrinos on Earth has been measured to be approximately 5×10^6 cm^{-2} s^{-1} [4,5], and its CEνNS has an energy spectrum hardly distinguishable from that of a 6 GeV/c^2 DM particle in LXe. No experimental determination of the solar neutrino flux using its CEνNS signal has been made yet. Recently, the XENON1T collaboration published a search for the ^{8}B CEνNS signal using 0.6 tonne year data with no excess found [6]. Because of the low nuclear recoil (NR) energy from the ^{8}B CEνNS, it is crucial to lower the energy threshold. In this Letter, we report a search for CEνNS induced by the solar ^{8}B neutrinos using the commissioning data of PandaX-4T (Run0) based on a blind analysis, with a dedicated data selection, which lowered the energy threshold (defined as the energy having signal acceptance of 1%) from 1.33 to 0.95 keV.

The PandaX-4T dark matter direct search experiment is located in the China Jinping underground laboratory (CJPL) [7,8]. The PandaX-4T experiment utilizes a dual-phase xenon time projection chamber (TPC) with a sensitive volume of 3.7 tonne of LXe, and two arrays of photomultipliers (PMTs) on the top and bottom of the TPC, consisting of 169 and 199 Hamamatsu 3-inch R11410-23 PMTs, respectively. Both the primary scintillation ($S1$) and the delayed proportional scintillation from drifted electrons ($S2$) of an event are collected by the PMTs, allowing 3D position reconstruction with a resolution of about a few millimeter for $S2$s of ~100 photoelectron (PE) on the longitudinal and transverse directions, based on the time difference between the $S1$ and $S2$, and the PMT pattern of the $S2$, respectively. The waveforms of the PMTs are digitized by CAEN V1725 digitizers and read out under the self-trigger mode when the pulse amplitude is approximately 1/3 PE above the baseline [9]. More details of the detector apparatus can be found in Refs. [9–11]. PandaX-4T has reported the most stringent constraint on the spin-independent cross sections between the nucleon and DM with the DM mass from 5 GeV/c^2 to 10 TeV/c^2 [10] using the 0.63-tonne-year data from Run0.

Compared with the search reported in Ref. [10], new data selections are developed to enhance the detection efficiency and to minimize the extra background that emerged from data. Thresholds of the $S1$ and $S2$ are lowered to 0.3 PE and 65 PE (both in charge), respectively, as compared with the 2 PE and 80 PE in Ref. [10]. The systematics of the background and the energy reconstruction at such a low threshold form the core of this analysis. With these thresholds, two sets of data used in Ref. [10] with a total live time of about 7.5 days show a higher noise rate, likely due to microdischarging in the TPC, and are removed from this analysis. The data selection cuts used in this analysis are described as follows. We adopt four selection cuts from the previous analysis [10], the diffusion cut ($S2$ widths compatible with the expected fluctuation on the electron arrival time), the veto PMT cut (no signal in the PMTs outside the field cage), the fiducial volume cut (FV, 2.67 tonnes), and the single scatter cut (only one $S2$ above 50 PE in the 1-ms event window). Events with large signals are observed to be followed by small afterglow signals in PandaX-4T and other experiments [12,13]. These afterglow signals usually are single electrons (SEs) which have a strong correlation with the previous large $S2$ in both time and position. Compared with Ref. [10], a more stringent afterglow veto based on the time and position difference to the previous event is implemented. Events with a time difference to previous $S2$ (> 2000 PE) less than 50 ms or position difference smaller than 100 mm are excluded. In addition, we veto the event unless the total charge per unit time and the number of $S1$s in the preceding 1-ms window have returned to normal. The afterglow veto cut also includes a set of "activity" requirements on an event waveform, that the ratio between the main $S2$ charge and the total event charge $\mathcal{F}_{S2} = q_{S2}/q_{\text{event}} > 5/6 - 150/q_{\text{event}}$, the integrated charge in the preceding event window to be less than 20 PE, and the main $S1$ to be the only signal within 4 μs around it. The effective live time of this analysis is estimated to be 64.7 days.

The signal expectation in this analysis is produced by a two-step simulation. The first step is the same as in Ref. [10], in which the correlated distributions in $S1$ and $S2$ are produced according to a fit to the calibration data, later referred to as the signal model. In the second step, a dedicated waveform simulation (WS) is developed. The waveform of the $S1$ is assembled using sampled $S1$ hits from the neutron calibration data, similar to the procedure in Ref. [14]. The waveform of the $S2$ at any given position

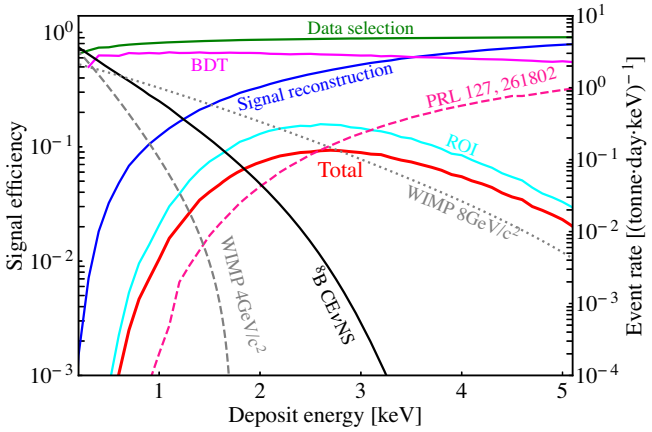

FIG. 1. Total efficiency (red solid line) to the solar ^{8}B neutrino CEνNS in this analysis with the number of $S1$ hits to be 2 or 3. The blue, green, cyan, and magenta solid lines represent the signal efficiencies due to the signal reconstruction, data selection, ROI, and BDT, respectively. The signal efficiency in the previous study [10] is also given in the pink dashed line as a reference. The ideal spectra of the solar ^{8}B CEνNS and the DM-nucleus interaction with the DM mass of $4(8)$ GeV/c^2 with an assumed DM-nucleon cross section of 10^{-44} cm^2 are overlaid as well in the black solid and gray dashed (dotted) curves, respectively, with the scale indicated on the right axis.

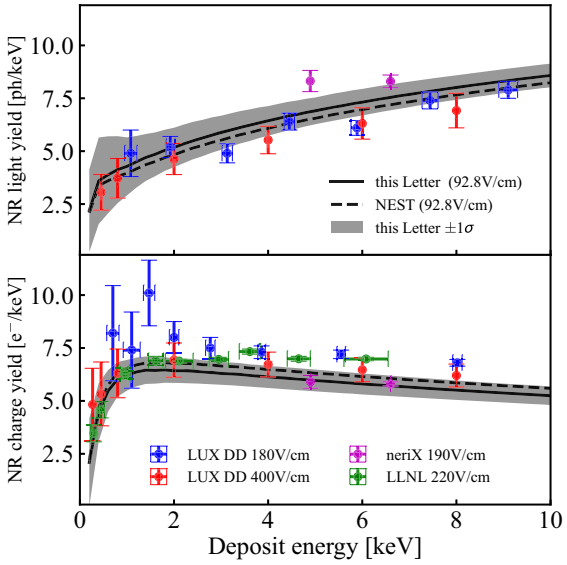

FIG. 2. Comparison between the light (top panel) and charge (bottom panel) yields used in this analysis (in the solid black lines) with the nominal NEST v2.3.6 [19] (dashed black lines) and other measurements taken at different drift electric fields [21–24]. The 1σ uncertainty from Ref. [20] for the light and charge yields are shown in the gray bands.

is assembled using individual SE waveforms from the data, with the reconstructed position within a 40-mm radius circle. The width of the overall assembled waveform at a given depth in the TPC is required to satisfy the diffusion relation observed from the data. Effects of PMT afterpulsing, delayed electrons [13,15–17], and photoionization of impurities after a large $S2$ are implemented in the WS according to the data. More details can be found in the Appendix.

The total efficiency to the ^{8}B CEνNS consists of four components (see Fig. 1): (1) the signal reconstruction, (2) the data selections discussed two paragraphs earlier, (3) the region of interest (ROI), and (4) a cut based on boosted decision tree (BDT, see later text). The signal reconstruction includes clustering of PMT hits into signal pulses, classification of the signal pulses into $S1$s and $S2$s, and pairing of the classified $S1$s and $S2$s into incident events. Each step of the signal reconstruction is affected by the presence of dark noises and stray electrons. For the ROI, we require the number of coincident PMT hits in an $S1$ to be either 2 or 3 in this analysis. The events with only a single-hit $S1$ are mostly accidental background originating from the PMT dark noises, and are excluded from the ROI due to a poor signal-to-background ratio. The $S2$ charge range, uncorrected for spatial dependence, is further optimized to be 65–230 PE for 2-hit $S1$ and 65–190 PE for 3-hit $S1$ based on the expected signal-to-background ratio. This ROI requirement has dominating effects on the signal efficiency. The efficiencies of (1), (2), and (3) are estimated using the WS and validated by the neutron calibration data, with their fractional difference (14%) taken as the systematic uncertainty.

We take the calculated deposit energy spectrum of the solar ^{8}B CEνNS in LXe from Ref. [18], which is shown in Fig. 1. The signal model implements the light and charge production in LXe following the NEST v2.3.6 parametrization [19], and the response of signal detection in the PandaX-4T detector, similar to Ref. [10]. The light and charge yields are extrapolated from the one used in Ref. [10], which has its model parameters fit to the neutron calibration data in the energy region of the DM search (see Fig. 2). We adopt the relative uncertainties of the light and charge yields from NEST [20], which is based on a global fit to all available measurements, and conservatively assume them to be uncorrelated.

The background composition is the same as Ref. [10]. With loosened $S1$ and $S2$ selections, the accidental coincidence (AC) background increases significantly in comparison to Ref. [10], which dominates the overall background. The electronic recoil (ER), NR, and surface background are estimated using the same method as in Ref. [10] but with the new data selections and the ROI cut.

The rate of the AC background is estimated using random $S1$s and $S2$s identified in the data. The $S2$s are first selected from a waveform (~1000 per day within 65 to 300 PE); then we search backward for 1.5 ms for a main $S1$. The 1.5-ms window is chosen so that the corresponding "activity" cuts are sufficiently similar to those mentioned earlier. The AC pair is formed when the time difference

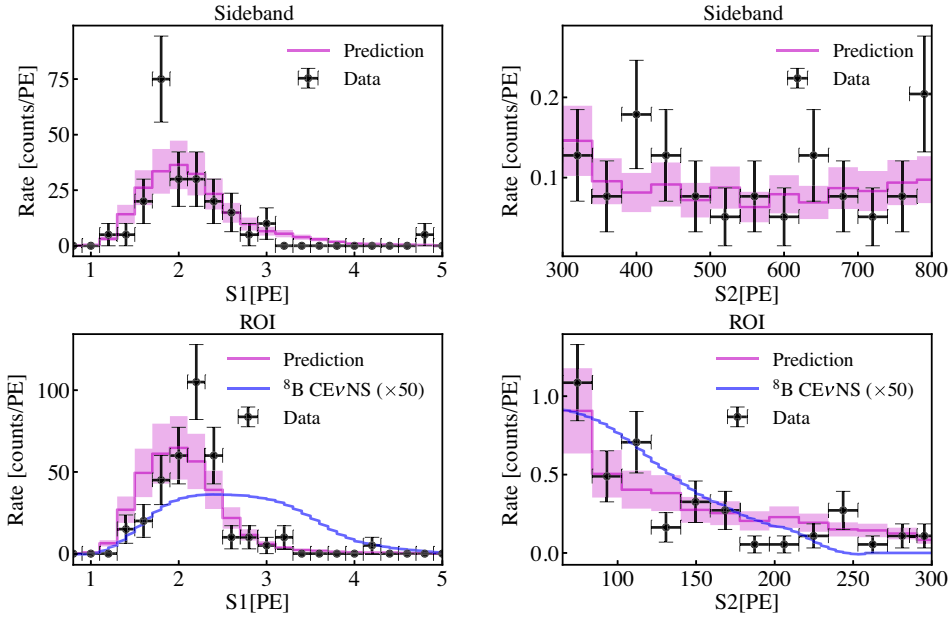

FIG. 3. The $S1$ (left panels) and $S2$ (right panels) spectra in the sideband (top panels) and ROI (bottom panels) for the 2-hit data, with the data and corresponding predictions overlaid. The shaded regions represent the 1σ uncertainty of the prediction (30%). We also overlay the expected ^{8}B CEνNS spectra (scaled up by 50) in the bottom panels, shown in blue solid lines. The goodness-of-fit p values of the $S1$ and $S2$ spectra in the sideband and ROI are all no less than 0.1.

between the $S1$ and $S2$ is within [0.9, 1.5] ms, beyond the TPC's maximum drift time (off window), to guarantee that there is no correlation. To enlarge the statistics of the AC samples, a "scrambled" waveform dataset is constructed. The waveform of the selected $S2$ is concatenated after a 1-ms segment randomly selected from our recorded data, which on average contains 6.3 (0.01) of the $S1$-like signals with the $S1$ hit equals to (larger than) 1, primarily from dark noises. This "scrambled" data get passed to the aforementioned software reconstruction and data selection. The predicted number of AC events in the ROI in the 2- and 3-hit regions can be found in Table I. The diffusion cut is the most effective cut, which suppresses the AC by a factor of 8 or so. The AC model is validated using the events with the $S2$ in the range from 300 to 800 PE (referred to as the sideband data) and within the FV, which is dominated by the AC (see Table II). The comparison between the sideband data and the prediction is given in Table II, yielding a good agreement. The comparison between the $S1$ and $S2$ spectra of the prediction and the sideband data for the 2-hit region is shown in Fig. 3. To be conservative, we take 30%, which is the difference (error-weighted standard deviation) in the normalized $S2$ spectra, as the systematic uncertainty of the AC model.

A BDT algorithm [25] is trained to optimize the ^{8}B CEνNS selection against the AC background. The $S2$s of the AC events are mostly generated out of the fiducial region (such as the surface of electrodes and the gas region), and the $S1$s are mostly dark noises (see Ref. [26]), both having different characters from the physical events. The input variables of the BDT concern features related to the charge, width, top-bottom asymmetry, and PMT top patterns of the $S1$ and $S2$ signals. The training and testing samples of the ^{8}B signal in the BDT are from the WS with the ($S1$, $S2$) distribution following our ^{8}B signal model. The BDT cut value and the $S2$ range for each $S1$ hit bin are determined by maximizing the probability of discovering a ^{8}B signal under our background model, with results summarized in Table I. The optimized BDT efficiency of the ^{8}B signal is shown in Fig. 1. The BDT

TABLE I. ROI comparison: Prediction vs observation in the optimized $S2$ ranges. The number of pre- and post-BDT events are listed in separate rows. The observed events after unblinding are shown in the last column.

N_{hit}	$S2$ range (PE)	BDT	ER	NR	Surface	AC	Total prediction	^{8}B	Observation
2	65–230	pre	0.04	0.10	0.14	62.43	62.71	2.32	**59**
		post	0.02	0.04	0.03	1.41	1.50	1.42	**1**
3	65–190	pre	0.01	0.05	0.08	0.79	0.93	0.42	**2**
		post	0.00	0.02	0.03	0.02	0.07	0.29	**0**

TABLE II. Sideband comparison: Prediction vs observation for $S2$ within [300, 800] PE.

N_{hit}	Physical	AC	Total	Observation
1	9.4	2060.5	2069.9	**2043**
2	10.1	33.8	43.9	**47**
3	6.9	2.2	9.1	**7**

reduces the ^{8}B CEνNS signal (AC background) by about 39% (98%) and 31% (96%), respectively, for the 2- and 3-hit bins. Most of the rejection power against the AC is gained through the parameters related to the $S2$ waveform shape and its top charge pattern, and we observe almost no correlation in the $S1$ and $S2$ discriminants. The uncertainties of the BDT efficiency to the ^{8}B CEνNS and the DM signals are studied using the neutron calibration data. To improve the statistics in the ROI, especially for $S2$ less than 100 PE, the minor $S2$s of the neutron double-scatter events are used. A difference of 14% and 13% are observed for the 2-hit and 3-hit ROI, respectively, taken as the systematic uncertainties. The systematic uncertainty of the BDT efficiency to the AC background is estimated by checking the performance on an alternative AC model using a more traditional approach based on the random pairing of the isolated $S1$s and $S2$s [26], leading to an uncertainty of 19% and 18% in the 2-hit and 3-hit bins.

The data within the ROI were blinded before we finalized the data selection, the background and signal models, the ROI, and the BDT optimization. We then unblinded the data and checked the events before and after applying the BDT. We show the comparison of the $S1$ and $S2$ spectra between the prediction and data before applying the BDT in Fig. 3. The observed number of the events in the ROI for the 2- and 3-hit regions are given in Table I. After unblinding, 1 (with $S1 = 1.6$ PE and $S2 = 165$ PE) and 0 events that survive the BDT are found in the 2- and 3-hit ROI, respectively.

We perform a simple statistical interpretation based on 2-bin profile likelihood ratio (PLR) analysis [27] using the 2- and 3-hit data. The binned likelihood is defined as [28]

$$\mathcal{L} = G(\delta_\epsilon)G(\delta_s)G(\delta_b)G(\delta_\Phi) \times \left[\prod_i G(\delta^i_{\mathrm{BDT},s})G(\delta^i_{\mathrm{BDT},b})\frac{\lambda_i^{N_i}}{N_i!}e^{-\lambda_i}\right], \quad (1)$$

where the index i represents the hit number of $S1$ (2 or 3), and $\boldsymbol{\delta}$ ($\boldsymbol{\delta^i}$) is series of the constrained nuisance parameters, which are correlated (independent) between the 2- and 3-hit bins with a Gaussian penalty G with the mean at zero. The set of parameters includes δ_ϵ, δ_s, δ_b, $\delta^i_{\mathrm{BDT},s}$, $\delta^i_{\mathrm{BDT},b}$, and δ_Φ, corresponding to the relative uncertainties of the pre-BDT efficiency (including the signal reconstruction, data selection, and ROI), the NR signal rate, the AC background rate, the BDT cut efficiency to the NR signals, the BDT efficiency to the AC background, and the ^{8}B neutrino flux, respectively. The 1σ values of the nuisance parameters are summarized in Table III. The parameter δ_s is factored together with the fractional uncertainty of the signal rate f_i which depends on the signal spectrum (f_i^ν for the ^{8}B CEνNS signal and f_i^χ for the DM signal), in order to reflect the common origin of f_i. Typical numbers of f_i are 0.45 (0.60), 0.29 (0.39), and 0.16 (0.24) for 4-GeV/c^2 DM, the ^{8}B CEνNS, and 8-GeV/c^2 DM in the 2-hit (3-hit) region. λ_i is the expected count while N_i is the observed count. Specifically, under the hypotheses of (a) the solar ^{8}B neutrino CEνNS without the DM, and (b) the low mass DM with the ^{8}B CEνNS background, the expected counts can be written as

$$\begin{aligned}\lambda_i^\nu &= N_\nu(1+\delta_s f_i^\nu)(1+\delta_\epsilon)(1+\delta^i_{\mathrm{BDT},s}) \\ &\quad + N_{\mathrm{AC}}(1+\delta_b)(1+\delta_\epsilon)(1+\delta^i_{\mathrm{BDT},b}) + N_{\mathrm{other}}, \\ \lambda_i^\chi &= N_\chi(1+\delta_s f_i^\chi)(1+\delta_\epsilon)(1+\delta^i_{\mathrm{BDT},s}) \\ &\quad + N_\nu(1+\delta_s f_i^\nu)(1+\delta_\epsilon)(1+\delta^i_{\mathrm{BDT},s})(1+\delta_\Phi) \\ &\quad + N_{\mathrm{AC}}(1+\delta_b)(1+\delta_\epsilon)(1+\delta^i_{\mathrm{BDT},b}) + N_{\mathrm{other}}, \end{aligned} \quad (2)$$

where N_ν, N_{AC}, N_{other}, and N_χ are the nominal numbers of counts for the ^{8}B CEνNS, AC, other background events (including ER and neutron), and low mass DM, respectively. The total backgrounds predicted in the 2- and 3-hit ROI for the solar ^{8}B neutrino search are 1.50 and 0.07, respectively, in an exposure of 0.48 tonne year, as shown in Table I. The observed number of events is consistent with both background-only hypotheses in searching for the ^{8}B CEνNS and the low mass DM in Eq. (2), representing a probability of 53% and 17% of observing the same or fewer number of events than the data, respectively.

Using a similar procedure as in Refs. [10,27], we give the 90% confidence level (C.L.) upper limit on the solar ^{8}B neutrino flux using the CEνNS channel, pushing the upper limit to $9.0 \times 10^6/\mathrm{cm}^2/\mathrm{s}$, in comparison to $(5.46 \pm 0.66) \times 10^6/\mathrm{cm}^2/\mathrm{s}$ from the standard solar model B16-GS98 [29].

TABLE III. List of the constrained nuisance parameters that are included in the final statistical interpretation (see text), along with the standard deviations (stdev.) of their Gaussian constraints.

Nuisance parameters		Stdev. 2-hit	Stdev. 3-hit	Estimated by
Pre-BDT efficiency	δ_ϵ	0.14		WS vs NR
NR signal rate	$\delta_s f_i$	f_i		NEST uncertainty [20]
AC rate	δ_b	0.30		Prediction vs sideband
BDT efficiency to signal	$\delta^i_{\mathrm{BDT},s}$	0.14	0.13	WS vs NR
BDT efficiency to AC	$\delta^i_{\mathrm{BDT},b}$	0.19	0.18	Alternative models [26]
Solar ^{8}B flux	δ_Φ	0.04		Ref. [5]

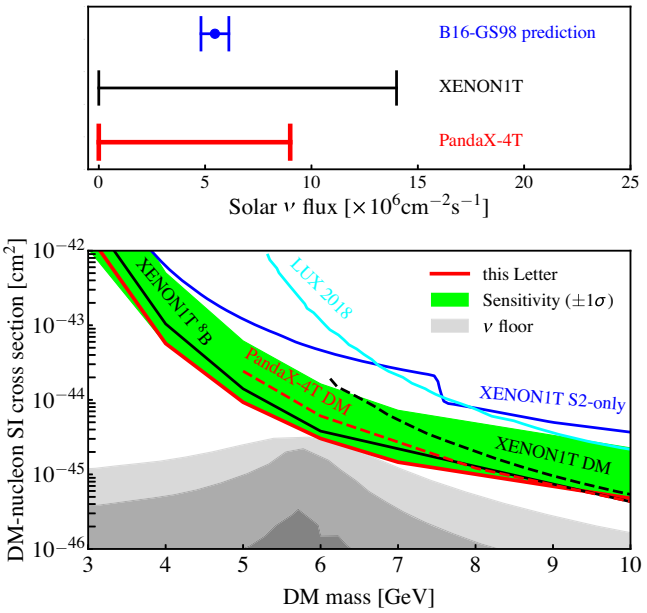

FIG. 4. Top panel: our constraint on the solar neutrino flux using the CEνNS analysis, along with the XENON1T results [6] using the same detection channel and the B16-GS98 standard solar model prediction [29]. Bottom panel: updated constraints on the DM-nucleon spin-independent cross section. The red solid and dashed lines represent the PandaX-4T results from this and the previous searches [10], respectively. The black solid and dashed lines represent the results from XENON1T with and without optimization in the low-energy region [6,30]. Several results from other experiments [31,32] are also shown. The neutrino floors (probability for an ideal xenon detector to see less-than-3σ-significance DM signal) [18] under different exposure assumptions (1, 10, and 1000 tonne-year from top to bottom) are shown in the gray shaded regions. The green region represents the $\pm 1\sigma$ sensitivity band for the DM search.

If the signal model adopted by XENON1T [6] is used, the upper limit of the solar ^{8}B neutrino flux will be lowered by 13%. If the signal model uncertainty (δ_s) is eliminated from the fit, the upper limit will be reduced by 10%. Under the nominal ^{8}B CEνNS rate, we also obtain the best constraints on the spin-independent DM-nucleon cross section with mass in the range of 3 to 9 GeV/c^2. The results are summarized in Fig. 4. In Fig. 4, we also show the ^{8}B neutrino floor curves from Ref. [18] under ideal background assumption. The current stage of PandaX has clearly entered into the sensitive region for neutrinos, so this result could also be cast into interesting parameter space of neutrino interactions. The lack of CEνNS excess from this Letter and XENON1T [6] also motivates further investigations on the response of LXe TPC to ultralow energy nuclear recoils.

In summary, a search for CEνNS from the solar ^{8}B neutrinos as well as the low-mass DM-nucleon interactions is performed using the PandaX-4T commissioning data with 0.48 tonne year exposure. In the analysis, we have further optimized the data selection and developed various techniques to lower the energy threshold and to control the accidental background. No significant excess is observed, leading to the strongest upper limit on the solar ^{8}B neutrino flux using CEνNS, and on the spin-independent DM-nucleon cross section within the mass range from 3 to 9 GeV/c^2. This manifests the potential of PandaX-4T as a highly sensitive multipurpose dark matter and astrophysical neutrino observatory.

We would like to thank Matthew Szydagis for useful discussions concerning NEST model uncertainty. This project is supported in part by grants from the National Natural Science Foundation of China (No. 1209061, No. 12005131, No. 11905128, and No. 11925502), a grant from the Ministry of Science and Technology of China (No. 2016YFA0400301), and by the Office of Science and Technology, Shanghai Municipal Government (Grant No. 18JC1410200). We are thankful for support from the Double First Class Plan of the Shanghai Jiao Tong University. We are also thankful for the sponsorship from the Chinese Academy of Sciences Center for Excellence in Particle Physics (CCEPP), Hongwen Foundation in Hong Kong, Tencent Foundation in China and Yangyang Development Fund. Finally, we thank the CJPL administration and the Yalong River Hydropower Development Company Ltd. for indispensable logistical support and other help.

Appendix: Waveform simulation.—To have sufficient high-purity samples for estimating the efficiency in the ROI and for training the BDT algorithm, a WS is developed, which includes our best knowledge from the data. The WS not only simulates the $S1$ and $S2$ pulses, but also simulates the accompanying noises that could appear in the event waveform, such as the PMT afterpulsing, the delayed electrons, the photoionization, and the spurious $S1$s [13,15–17].

The simulation of the $S1$ and $S2$ pulse waveforms is data driven. The simulated $S1$ pulse waveform is sampled using the real $S1$ hits from the neutron calibration data with the charge from 20 to 80 PE. The width distribution of the simulated $S1$s and $S1$s from the neutron calibration data in the ROI can be found in the top panel of Fig. 5. The simulated $S2$ pulse waveform is reassembled using the SE waveforms obtained from the data. The SEs are sampled within a circle with a radius $R_0 = 40$ mm based on their reconstructed positions. R_0 is tuned to match the root-mean-square distance of all fired top PMTs, weighted by charge, from the position of the top PMT that sees the most $S2$ charge (σ_{pos}). With $R_0 = 40$ mm, the comparison of σ_{pos} between the neutron calibration data and WS are shown in the middle panel of Fig. 5. The pileup of the SEs is required to follow a Gaussian distribution with the Gaussian σ equal to $\sqrt{2DT}$, where D is the longitudinal diffusion coefficient in LXe and T is the drift time of the simulated $S2$. The value of D is obtained to be 28 cm^2/s by matching the $S2$

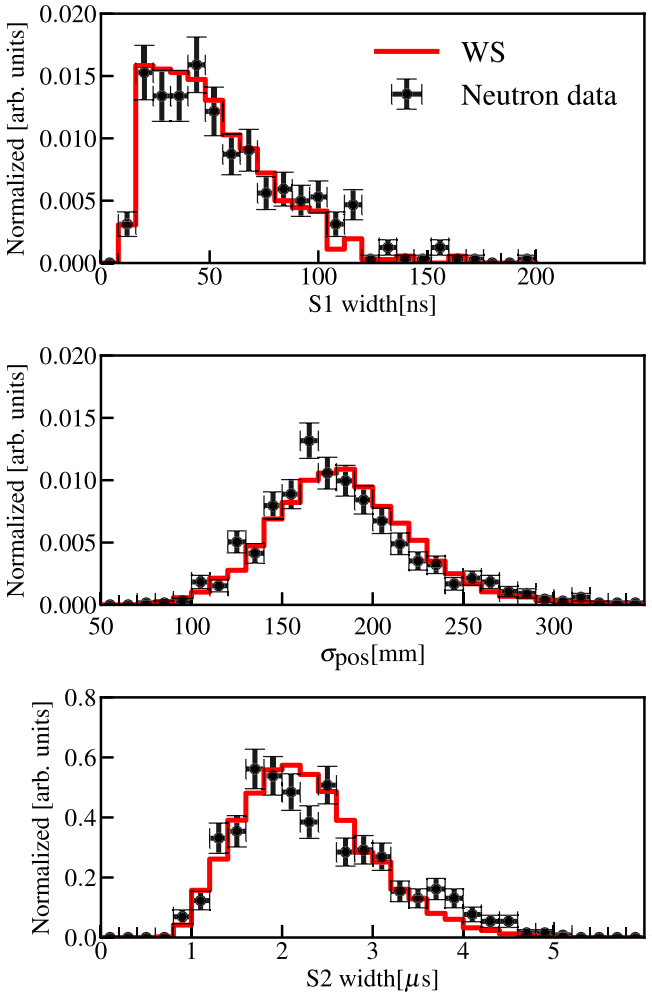

FIG. 5. The comparisons between the neutron calibration data and WS of $S1$ width (top), σ_{pos} (middle), and $S2$ width (bottom) normalized distributions in the ROI.

width vs drift time distribution of the neutron calibration data. The comparison of the $S2$ width distribution between the neutron calibration data and WS in the ROI can be found in the bottom panel of Fig. 5.

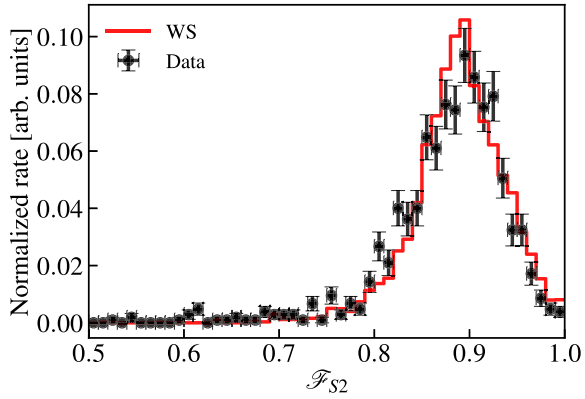

FIG. 6. Comparison between the $\mathcal{F}_{S2}$ distributions from the WS (red solid line) and data (black dots with error bars).

Dark counts and noises are included by inserting randomly picked 1-ms-long waveforms from all the recorded waveforms into the simulated event window. PMT afterpulsing are already included, since the simulated $S1$ and $S2$ are both sampled using the waveforms from the data. Delayed electrons and impurity photoionization can cause small delayed $S2$ signals after a large $S2$. The time profile and probability of such delayed $S2$s are obtained by analyzing the data waveforms after the main $S2$. The parameter which is mostly sensitive to the noise and afterglows is the $\mathcal{F}_{S2}$ that is defined in the main text. Figure 6 shows the comparison between the $\mathcal{F}_{S2}$ distributions from the neutron calibration data and the WS.

*Corresponding author.
qinglin@ustc.edu.cn
†Spokesperson: jianglai.liu@sjtu.edu.cn
‡Corresponding author.
mengyue@sjtu.edu.cn

[1] E. Aprile, J. Aalbers, F. Agostini, M. Alfonsi, L. Althueser, F. Amaro, V. C. Antochi, E. Angelino, J. Angevaare, F. Arneodo *et al.*, Projected wimp sensitivity of the XENONnT dark matter experiment, J. Cosmol. Astropart. Phys. 11 (2020) 031.

[2] D. Akerib, C. Akerlof, S. Alsum, H. Araújo, M. Arthurs, X. Bai, A. Bailey, J. Balajthy, S. Balashov, D. Bauer *et al.*, Projected wimp sensitivity of the LUX-ZEPLIN dark matter experiment, Phys. Rev. D **101**, 052002 (2020).

[3] H. Zhang, A. Abdukerim, W. Chen, X. Chen, Y. Chen, X. Cui, B. Dong, D. Fang, C. Fu, K. Giboni *et al.*, Dark matter direct search sensitivity of the PandaX-4T experiment, Sci. China Phys. Mech. Astron. **62**, 31011 (2019).

[4] M. Agostini, K. Altenmüller, S. Appel, D. Jeschke, B. Neumair, L. Oberauer, L. Papp, S. Schönert, F. von Feilitzsch, V. Atroshchenko *et al.*, Comprehensive measurement of pp-chain solar neutrinos, Nature (London) **562**, 505 (2018).

[5] B. Aharmim, S. Ahmed, A. Anthony, N. Barros, E. Beier, A. Bellerive, B. Beltran, M. Bergevin, S. Biller, K. Boudjemline *et al.*, Combined analysis of all three phases of solar neutrino data from the sudbury neutrino observatory, Phys. Rev. C **88**, 025501 (2013).

[6] E. Aprile, J. Aalbers, F. Agostini, S. A. Maouloud, M. Alfonsi, L. Althueser, F. Amaro, S. Andaloro, V. C. Antochi, E. Angelino *et al.*, Search for Coherent Elastic Scattering of Solar 8B Neutrinos in the XENON1T Dark Matter Experiment, Phys. Rev. Lett. **126**, 091301 (2021).

[7] K.-J. Kang, J.-P. Cheng, Y.-H. Chen, Y. Li, M. Shen, S. Wu, and Q. Yue, *Status and prospects of a deep underground laboratory in china*, in Journal of Physics: Conference Series, Vol. 203 (IOP Publishing, 2010), p. 012028.

[8] J. Li, X. Ji, W. Haxton, and J. S. Wang, The second-phase development of the china jinping underground laboratory, Phys. Procedia **61**, 576 (2015).

[9] C. He, J. Liu, X. Ren, X. Shang, X. Wei, M. Wang, J. Yang, Y. Yang, G. Zhang, and Q. Zheng, A 500 ms/s waveform

digitizer for pandax dark matter experiments, J. Instrum. **16**, T12015 (2021).
[10] Y. Meng, Z. Wang, Y. Tao, A. Abdukerim, Z. Bo, W. Chen, X. Chen, Y. Chen, C. Cheng, Y. Cheng *et al.*, Dark Matter Search Results from the PandaX-4T Commissioning Run, Phys. Rev. Lett. **127**, 261802 (2021).
[11] L. Zhao, X. Cui, W. Ma, Y. Fan, K. Giboni, T. Zhang, J. Liu, and X. Ji, The Cryogenics and Xenon handling system for the PandaX-4T experiment, J. Instrum. **16**, T06007 (2021).
[12] E. Aprile *et al.* (XENON100 Collaboration), Observation and applications of single-electron charge signals in the XENON100 experiment, J. Phys. G **41**, 035201 (2014).
[13] D. Akerib, S. Alsum, H. Araújo, X. Bai, J. Balajthy, A. Baxter, E. Bernard, A. Bernstein, T. Biesiadzinski, E. Boulton *et al.*, Investigation of background electron emission in the LUX detector, Phys. Rev. D **102**, 092004 (2020).
[14] D. Akerib, C. Akerlof, A. Alqahtani, S. Alsum, T. Anderson, N. Angelides, H. Araújo, J. Armstrong, M. Arthurs, X. Bai *et al.*, Simulations of events for the LUX-zeplin (lz) dark matter experiment, Astropart. Phys. **125**, 102480 (2021).
[15] P. Sorensen and K. Kamdin, Two distinct components of the delayed single electron background signals in liquid xenon emission detectors, J. Instrum. **13**, P02032 (2018).
[16] P. Sorensen, Electron train backgrounds in liquid xenon dark matter search detectors are indeed due to thermalization and trapping, arXiv:1702.04805.
[17] D. Akerib, S. Alsum, H. Araújo, X. Bai, J. Balajthy, J. Bang, A. Baxter, E. Bernard, A. Bernstein, T. Biesiadzinski *et al.*, Improving sensitivity to low-mass dark matter in LUX using a novel electrode background mitigation technique, Phys. Rev. D **104**, 012011 (2021).
[18] F. Ruppin, J. Billard, E. Figueroa-Feliciano, and L. Strigari, Complementarity of dark matter detectors in light of the neutrino background, Phys. Rev. D **90**, 083510 (2014).
[19] M. Szydagis, J. Balajthy, J. Brodsky, J. Cutter, J. Huang, E. Kozlova, B. Lenardo, A. Manalaysay, D. McKinsey, M. Mooney *et al.*, *Noble element simulation technique v2. 0*, (Zenodo, Geneve, Switzerland, 2018).
[20] M. Szydagis, The noble element simulation technique (nest): Recent updates and improvements, Bull. Am. Phys. Soc. (2022), https://meetings.aps.org/Meeting/APR22/Session/W09.6.
[21] D. Akerib, S. Alsum, H. Araújo, X. Bai, A. Bailey, J. Balajthy, P. Beltrame, E. Bernard, A. Bernstein, T. Biesiadzinski *et al.*, Low-energy (0.7–74 kev) nuclear recoil calibration of the LUX dark matter experiment using dd neutron scattering kinematics, arXiv:1608.05381.
[22] D. Huang, Ultra-low energy calibration of the LUX and LZ dark matter detectors, Ph. D. Thesis, Brown University, 2020.
[23] E. Aprile, M. Anthony, Q. Lin, Z. Greene, P. de Perio, F. Gao, J. Howlett, G. Plante, Y. Zhang, and T. Zhu, Simultaneous measurement of the light and charge response of liquid xenon to low-energy nuclear recoils at multiple electric fields, Phys. Rev. D **98**, 112003 (2018).
[24] B. Lenardo, J. Xu, S. Pereverzev, O. A. Akindele, D. Naim, J. Kingston, A. Bernstein, K. Kazkaz, M. Tripathi, C. Awe *et al.*, Measurement of the ionization yield from nuclear recoils in liquid xenon between 0.3–6 kev with single-ionization-electron sensitivity, arXiv:1908.00518.
[25] A. Hoecker, P. Speckmayer, J. Stelzer, J. Therhaag, E. von Toerne, H. Voss, M. Backes, T. Carli, O. Cohen, A. Christov *et al.*, Tmva-toolkit for multivariate data analysis, arXiv:physics/0703039.
[26] A. Abdukerim, W. Chen, X. Chen, Y. Chen, C. Cheng, X. Cui, Y. Fan, D. Fang, C. Fu, M. Fu *et al.*, Study of background from accidental coincidence signals in the Pandax-II experiment, Chin. Phys. C **46**, 103001 (2022).
[27] D. Baxter, I. Bloch, E. Bodnia, X. Chen, J. Conrad, P. Di Gangi, J. Dobson, D. Durnford, S. Haselschwardt, A. Kaboth *et al.*, Recommended conventions for reporting results from direct dark matter searches, Eur. Phys. J. C **81**, 907 (2021).
[28] Penalty term $G(\delta_\Phi)$ is not used when interpreting results under the signal hypothesis of solar ^{8}B CEνNS.
[29] N. Vinyoles, A. M. Serenelli, F. L. Villante, S. Basu, J. Bergström, M. Gonzalez-Garcia, M. Maltoni, C. Peña-Garay, and N. Song, A new generation of standard solar models, Astrophys. J. **835**, 202 (2017).
[30] E. Aprile, J. Aalbers, F. Agostini, M. Alfonsi, L. Althueser, F. Amaro, M. Anthony, F. Arneodo, L. Baudis *et al.* (X. Collaboration), Dark Matter Search Results from a One Ton-Year Exposure of XENON1T, Phys. Rev. Lett. **121**, 111302 (2018).
[31] E. Aprile, J. Aalbers, F. Agostini, M. Alfonsi, L. Althueser, F. Amaro, V. C. Antochi, E. Angelino, F. Arneodo, D. Barge *et al.*, Light Dark Matter Search with Ionization Signals in XENON1T, Phys. Rev. Lett. **123**, 251801 (2019).
[32] D. Akerib, S. Alsum, H. Araújo, X. Bai, A. Bailey, J. Balajthy, P. Beltrame, E. Bernard, A. Bernstein, T. Biesiadzinski *et al.*, Results from a Search for Dark Matter in the Complete LUX Exposure, Phys. Rev. Lett. **118**, 021303 (2017).